Research Article | Open Access

Microstructures

Choi *et al*. *Microstructures* **2026**, *6*, 2026071 **DOI:**10.20517/microstructures.2025.169

Stoichiometry- and lattice-tunable MoN_x as a novel electrode platform for ferroelectric $Hf_{0.5}Zr_{0.5}O_2$ capacitors

Hyojun Choi[1], Ju Yong Park[1], Jaewook Lee[1], Hyun Woo Jeong[1], Kun Yang[1], Sun Young Lee[1], Dong In Han[1], Heejin Hong[1], Young Yong Kim[2], Min Hyuk Park[1,3]

Keywords: Ferroelectric $Hf_{0.5}Zr_{0.5}O_2$, molybdenum nitride, interface engineering, wake-up effect, cycling endurance, oxidation resistance

Citation: Choi, H.; Park, J. Y.; Lee, J.; Jeong, H. W.; Yang, K.; Lee, S. Y.; Han, D. I.; Hong, H.; Kim, Y. Y.; Park, M. H. Stoichiometry- and lattice-tunable MoN_x as a novel electrode platform for ferroelectric $Hf_{0.5}Zr_{0.5}O_2$ capacitors. *Microstructures* **2026**, *6*, 2026071. https://dx.doi.org/10.20517/microstructures.2025.169

Received: 18 Dec 2025 **First Decision:** 27 Feb 2026 **Revised:** 1 May 2026 **Accepted:** 13 May 2026 **Published:** 27 May 2026

Academic Editor: Dawei Wang **Copy Editor:** Shu-Yuan Duan **Production Editor:** Shu-Yuan Duan

Check for updates

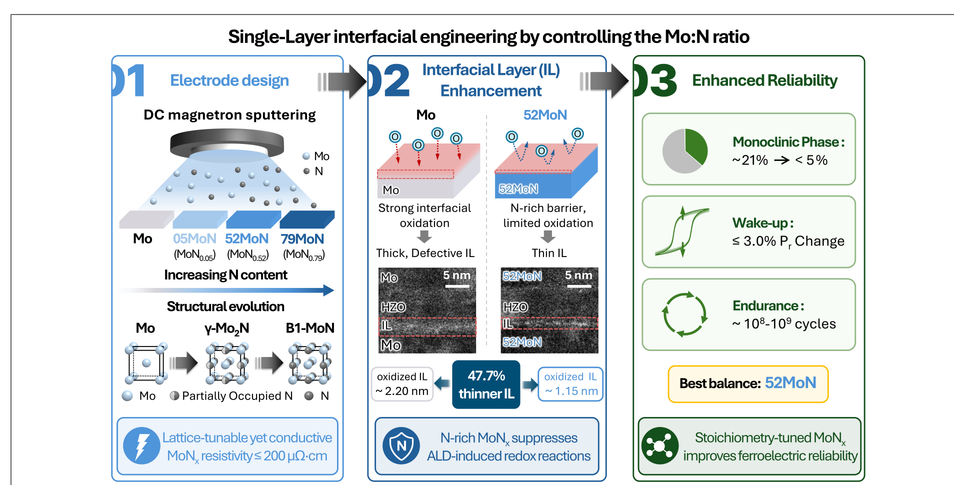

Abstract

Ferroelectricity in $(Hf,Zr)O_2$ thin films is highly sensitive to bottom-electrode chemistry, as interfacial redox reactions during atomic layer deposition (ALD) and subsequent annealing can generate defective interlayers and alter oxygen-vacancy distributions. Here, we propose a stoichiometry- and lattice-tunable molybdenum nitride (MoN_x) electrode platform that enables single-layer interfacial engineering through control of the Mo:N ratio. MoN_x films with x = 0.00, 0.05, 0.52, and 0.79 (denoted as Mo, 05MoN, 52MoN, and 79MoN) were sputter-deposited and integrated into symmetric $MoN_x/Hf_{0.5}Zr_{0.5}O_2/MoN_x$ capacitors containing 8 nm-thick ALD $Hf_{0.5}Zr_{0.5}O_2$. Structural analysis confirms a transition from Mo (110)-textured films to rock-salt-type MoN_x with a (111) texture at higher N contents, while electrode-grade resistivity is maintained (≤ 200 μΩ•cm for 52MoN). Chemical analyses reveal that increasing the N content substantially suppresses ALD-induced electrode oxidation and reduce the thickness of the oxidized interfacial-layer

[1]Department of Materials Science and Engineering, Inter-University Semiconductor Research Center, and Research Institute of Advanced Materials, College of Engineering, Seoul National University, Seoul 08826, Republic of Korea.
[2]Beamline Division, Pohang Accelerator Laboratory, Pohang University of Science & Technology, Pohang 37673, Republic of Korea.
[3]Institute of Engineering Research, College of Engineering, Seoul National University, Seoul 08826, Republic of Korea.

Correspondence to: Prof. Min Hyuk Park, Department of Materials Science and Engineering, Inter-University Semiconductor Research Center, Research Institute of Advanced Materials, and Institute of Engineering Research, College of Engineering, Seoul National University, Seoul 08826, Republic of Korea. E-mail: minhyuk.park@snu.ac.kr

by 47.7% for 52MoN relative to Mo; N incorporation into the $Hf_{0.5}Zr_{0.5}O_2$ (HZO) near the bottom interface is also detected. Consistently, the monoclinic phase fraction decreases from ~ 21% for Mo to < 5% for 52MoN and 79MoN. All capacitors exhibit minimal wake-up, with a ≤ 3.0% change in double remanent polarization after 10^4 cycles at 3 MV•cm^{-1}. Benchmarking against other stoichiometry-controlled electrode systems (e.g., TaN_x, RuO_x, and TiN_x) shows that the MoN_x platform maintains high pristine polarization (> 47.5 μC•cm^{-2}) while suppressing wake-up across a wide compositional range. Endurance improves markedly with N content, reaching ~ 10^8-10^9 cycles for high-N MoN_x electrodes, depending on the cycling voltage. These results establish MoN_x as a scalable, composition-engineerable electrode system that couples interfacial microstructure control with enhanced ferroelectric reliability in HZO thin films.

INTRODUCTION

Ferroelectricity in $(Hf,Zr)O_2$ thin films has attracted substantial academic and industrial interest since its first report in 2011[1], driven by its potential for next-generation high-density semiconductor memories and emerging computing hardware. $Hf_{0.5}Zr_{0.5}O_2$ (HZO) is highly compatible with complementary metal-oxide-semiconductor (CMOS) processing, and atomic layer deposition (ALD) enables uniform ultrathin films in which remanent polarization (P_r) can exceed ~ 15 μC·cm^{-2} even at thickness below 5 nm[2-5]. Together with switching endurance that has been improved toward and beyond 10^{12} cycles, $Hf_{0.5}Zr_{0.5}O_2$ has become a leading candidate for ferroelectric random-access memory (FeRAM), ferroelectric field-effect transistors (FeFETs), and ferroelectric tunnel junctions (FTJs)[6-9]. In particular, FeRAM and FeFET concepts are being actively pursued as promising future technologies for advanced DRAM and 3D NAND[3-5,9-13].

A key integration challenge is that ferroelectricity in vacuum-processed $Hf_{0.5}Zr_{0.5}O_2$ films is strongly governed by the bottom electrode[14-16]. The electrode crystal structure, work function, and microstructure, together with its chemical properties that control interfacial redox reactions, have all been reported to affect $Hf_{0.5}Zr_{0.5}O_2$ phase stability, oxygen-vacancy (V_o) distributions, wake-up behavior, and endurance.

Mo has emerged as a next-generation metal for advanced interconnects as dimensional scaling proceeds and the shortened electron mean free path penalizes incumbent low-resistivity conductors such as Cu and W in ultrathin regimes. Notably, W word lines in 3D NAND flash are already being replaced by Mo[17-19]. This transition is motivated by the lower resistivity of Mo in ultrathin films, the potential to reduce or avoid barrier-layer use and thereby lower line resistance, and the feasibility of conformal film formation in three-dimensional nanostructures by ALD. Consequently, Mo and Mo-based compounds, including MoO_x and molybdenum nitrides (MoN_x), are increasingly considered not only as line/interconnect materials but also as electrode candidates for advanced device stacks[20-23].

Mo is also attractive as an electrode for ferroelectric $(Hf,Zr)O_2$[24-26]. Its relatively high work function (~ 4.7-4.9 eV[27,28]) is sufficient to suppress leakage current. In addition, prior studies have suggested that Mo does not strongly scavenge O from $(Hf,Zr)O_2$; rather, because Mo-O bonding is weaker than Hf-O or Zr-O bonding, Mo can supply O to $(Hf,Zr)O_2$ and decrease V_o concentration. This behavior can suppress interfacial tetragonal-phase formation driven by high V_o concentrations and significantly mitigate wake-up. However, during ALD of $(Hf,Zr)O_2$, strong oxidants such as ozone can oxidize Mo and form a defective MoO_x interlayer, degrading leakage characteristics and switching endurance.

Mo-based compound electrodes, such as MoO_x and MoN_x, are therefore promising alternatives for addressing the limitations of elemental Mo. Since these compounds remain Mo-based, oxygen scavenging and the subsequent V_o formation in $(Hf,Zr)O_2$ are expected to be minimal. Furthermore, the incorporated O or N may improve resistance to further surface oxidation during exposure to ALD oxygen sources. Among

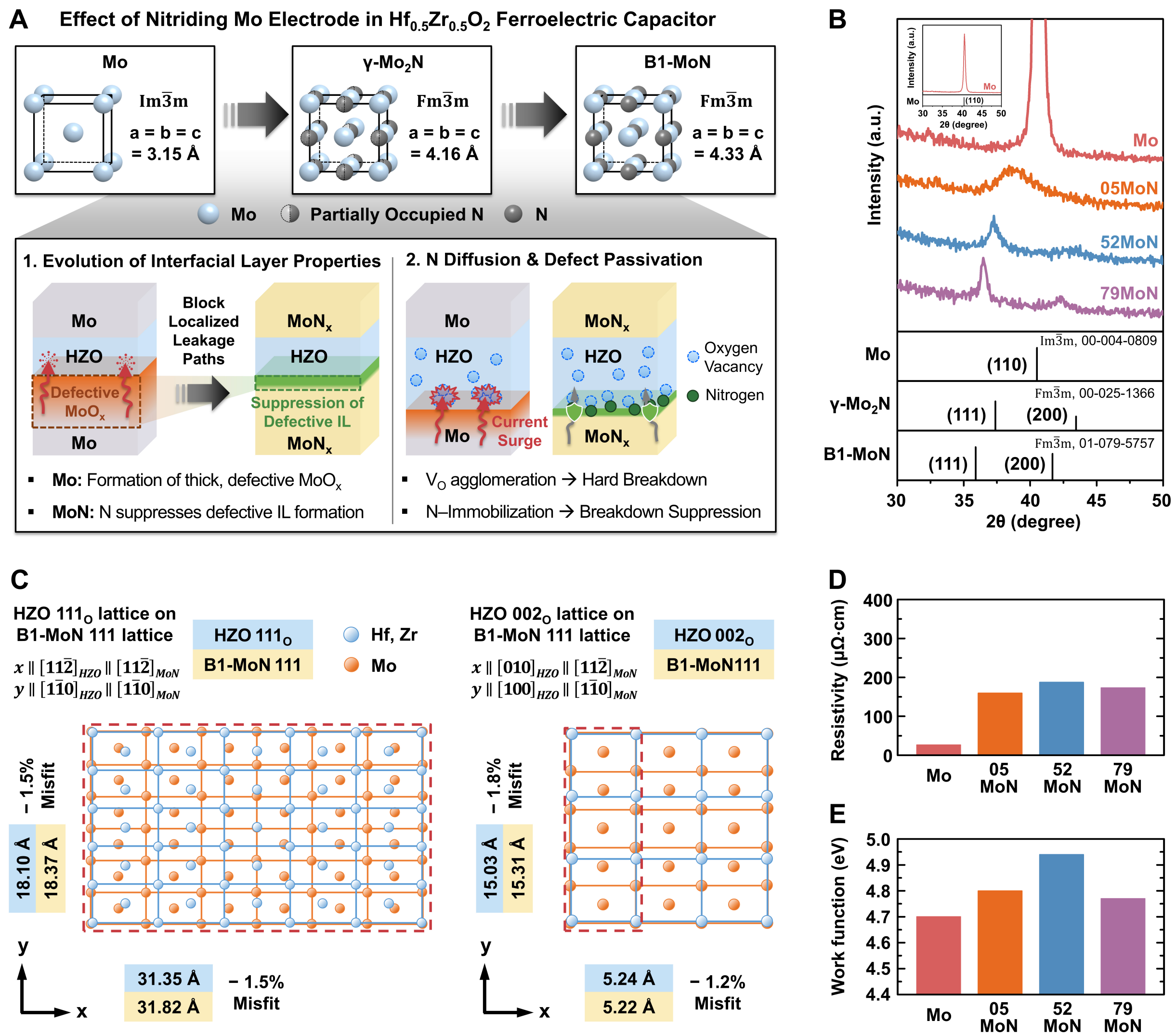

Figure 1. Effect of electrode nitridation on interfacial microstructure and electrical properties. (A) Schematic illustrations depict the phase evolution from body-centered cubic Mo to rock-salt-type MoN_x and the corresponding reliability mechanisms; (B) X-ray diffraction patterns of Mo, 05MoN, 52MoN, and 79MoN thin films. The inset displays the full-scale intensity of the pure Mo film, showing the untruncated Mo (110) diffraction peak; (C) Lattice-matching models were constructed to evaluate the compatibility between orthorhombic $Hf_{0.5}Zr_{0.5}O_2$ (HZO) (111), denoted as 111O and B1-MoN (111). The supercells, indicated by red dashed boxes, represent a 5:6 domain-matching configuration (left) and a 3:5 matching configuration (right); Electrical characteristics evaluated by (D) four-point probe resistivity measurements and (E) work function (Φ) values extracted from ultraviolet photoelectron spectroscopy.

Mo oxides, MoO_2 is potentially advantageous because of its high work function and expected favorable interfacial compatibility with HZO[24,29]. However, additional oxidation can yield MoO_3; because MoO_3 is a wide-bandgap semiconductor[30], its formation can substantially degrade electrode functionality.

MoN_x compounds offer a particularly compelling route because they can preserve the weak oxygen-scavenging characteristics of Mo while mitigating ALD-induced surface oxidation. Importantly, MoN_x provides a broad stoichiometric window with closely related crystal structures. As illustrated in Figure 1A, B1-MoN (Mo:N = 1:1) adopts a rock-salt-type ($Fm\bar{3}m$) structure with a lattice parameter of ~ 0.436 nm and metallic character. γ-Mo_2N (Mo:N = 2:1) has a closely related structure in which only ~ 50% of the anion sites are occupied, with a lattice parameter of ~ 0.416 nm. Thus, within Mo:N ratios from ~ 2:1 to 1:1, MoN_x can remain metallic while enabling lattice-parameter tuning from ~ 0.416 to ~ 0.436 nm. Reported work functions for γ-Mo_2N and B1-MoN span 4.4-5.3 eV[31-36], suggesting that electrode energetics may also be tunable via stoichiometry.

In this study, we propose MoN_x as a compound-electrode material platform that enables both (i) interfacial engineering through oxidation resistance and redox/transport control and (ii) potential texture engineering through stoichiometry-dependent lattice-parameter tuning. By sputtering MoN_x electrodes with different Mo:N ratios and integrating them as bottom electrodes in ferroelectric HZO capacitors, we demonstrate that the defective interfacial layer (IL) formed during ALD can be substantially reduced. Suppressed oxygen scavenging and partial O/N supply effects reduce non-ferroelectric monoclinic-phase formation, lower the coercive field (E_c), mitigate wake-up, improve endurance, and measurably alter the HZO microstructure. The MoN_x bottom-electrode system introduced here provides immediate performance gains and a scalable pathway for further optimization through compositional and microstructural engineering.

MATERIALS AND METHODS

Sample fabrication

Deposition of Mo and MoN_x electrodes

To investigate the effect of nitrogen (N) incorporation on the ferroelectric properties, MoN_x bottom electrodes were deposited on p-type Si substrates (resistivity: 1-10 Ω·cm; thickness: ~ 675 μm) using a DC magnetron co-sputtering system (Daeki Hi-Tech, Republic of Korea). A Mo target (3 inch diameter, 99.95% purity; Thifine, Republic of Korea) was used for both the pure Mo and MoN_x depositions. Before N-content modulation, a pure Mo reference electrode was deposited under fixed conditions of 150 W DC power, 1 mTorr working pressure, and an Ar gas flow of 11 sccm. For the MoN_x electrodes, deposition was performed at a fixed DC power of 150 W and a working pressure of 2 mTorr. To control stoichiometry precisely, the total gas flow rate was maintained at 40 sccm, while the N_2/Ar flow ratios were varied as 2/38, 8/32, and 20/20 sccm, corresponding to gas-phase N_2 fractions of 5%, 20%, and 50%, respectively. All bottom and top electrodes were deposited to a thickness greater than 20 nm to eliminate thickness-dependent variations in electrode properties.

HZO deposition and capacitor fabrication

An 8 nm-thick solid-solution HZO thin film was then deposited by thermal ALD (iOV-mX1, ISAC Research, Republic of Korea) at a substrate temperature of 280 °C. Before HZO growth, a 10 min stabilization step was applied for both Mo and MoN_x electrodes to ensure that the ALD chamber and substrate reached thermal equilibrium. $Hf[N(C_2H_5)CH_3]_4$ (TEMAHf, iChems, Republic of Korea) and $Zr[N(C_2H_5)CH_3]_4$ (TEMAZr, iChems, Republic of Korea) were used as the Hf and Zr precursors, respectively, and O_3 with a density of 200 $g{\cdot}m^{-3}$, generated using an ozone generator (CN-1, Ozone Tech, Republic of Korea), served as the oxidant. Each HfO_2 or ZrO_2 subcycle consisted of a TEMAHf (2.0 s) or TEMAZr (2.5 s) pulse, a 12 s purge, a 3.0 s O_3 pulse, and a subsequent 12 s purge. The thickness and composition of the deposited HZO films were verified using X-ray fluorescence spectroscopy (XRF, ARL Quant'X, Thermo Scientific, USA). To fabricate symmetric metal-ferroelectric-metal (MFM) capacitors, MoN_x top electrodes were deposited under the same sputtering conditions as the bottom electrodes. Capacitor areas were defined using physical shadow masks with a dimensions of 75 × 75 μm^2. Finally, all capacitors underwent a rapid thermal processing (RTP, Real RTP 100, ULTECH, Republic of Korea) at 400 °C under an N_2 atmosphere (~ 10 Torr) with a ramp rate of ~ 25 °C·s^{-1} and a hold time of 180 s to crystallize the HZO films.

Sample preparation for chemical and structural analysis

To elucidate the origins of the electrical differences and isolate bottom-interface reactions, simplified stacks consisting of 8 or 2.5 nm HZO deposited on Mo or MoN_x bottom electrodes (without top electrodes) were separately fabricated for X-ray photoelectron spectroscopy (XPS, Axis Supra$^+$, Kratos Analytical, Japan) and time-of-flight secondary ion mass spectrometry (ToF-SIMS, TOF-SIMS-5, ION-TOF, Germany),

respectively. The thinner 2.5 nm HZO samples were specifically prepared to enhance XPS sensitivity to the buried interface. For microstructural characterization of the crystallized HZO films by atomic force microscopy (AFM, NX-10, Park Systems, Republic of Korea), field-emission scanning electron microscopy (FE-SEM, SU8010, Hitachi High-Tech, Japan), and grazing-incidence X-ray diffraction (GIXRD, X'pert Pro, PANalytical, Netherlands), the top MoN_x electrodes were selectively removed from the fully processed MFM capacitors using an SC-1 wet etching solution ($NH_4OH:H_2O_2:H_2O$ = 1:2:50 by volume at 50 °C). This process exposed the underlying HZO surface without altering the thermal history of the HZO film.

Sample characterization

Electrical and ferroelectric measurements

The ferroelectric properties of the fabricated capacitors were evaluated using an ultra-fast pulse measurement unit (4225-PMU, Keithley, USA) embedded in a semiconductor parameter analyzer (4200A-SCS, Keithley, USA). Polarization-electric field (P-E) hysteresis loops were obtained by applying bipolar triangular pulses with varying amplitudes at a frequency of 1 kHz. For reliability assessment, endurance tests were conducted using bipolar rectangular pulses at 100 kHz. To accurately extract P_r and E_c, positive-up-negative-down (PUND) measurements were performed to exclude non-ferroelectric contributions such as leakage current and dielectric response. The electrical resistivity of the electrodes was measured using a four-point-probe system (CMT-SR1000N, Chang Min Co., Ltd., Republic of Korea).

Chemical composition and depth profiling

The chemical bonding states and compositions of the MoN_x electrodes were analyzed using XPS (Axis Supra$^+$, Kratos). The work function was determined by ultraviolet photoelectron spectroscopy (UPS) using a He I discharge lamp (hν = 21.22 eV). To examine elemental depth distributions and interfacial diffusion, ToF-SIMS depth profiling was performed using a Bi^+ primary ion beam and a Cs^+ sputtering beam.

Crystallographic structure and texture analysis

Surface morphology and roughness were characterized by AFM. The crystal structures of the MoN_x electrodes and HZO films were investigated using Bragg-Brentano X-ray diffraction (XRD, D8 Advance, Bruker, USA) and GIXRD, respectively. The 2θ scanning range was 25°-45°, with an incident angle (ω) of 0.5°. The step size and counting time were 0.05° and 3 s, respectively. To examine the crystal structure and preferred orientation of the HZO thin films deposited on Mo and MoN_x electrodes, grazing-incidence wide-angle X-ray scattering (GIWAXS) measurements were conducted at the 3C beamline of the Pohang Light Source-II (PLS-II). The incident X-ray beam was irradiated onto the sample surface at a grazing-incidence angle of 0.5°, which was selected to maximize scattering from the HZO thin film while minimizing the substrate background. The scattered X-rays were detected using a 2D area detector (Eiger X4M, Dectris, Switzerland) with an exposure time of 30 s for each sample. The obtained 2D diffraction images were calibrated and converted into reciprocal-space maps (q_{xy} *vs.* q_z) using PGIXS software. Because the 2D detector captures diffracted photons as functions of both azimuthal angle and 2θ, the resulting GIWAXS patterns exhibit Debye-Scherrer rings, enabling comprehensive analysis of texture and phase evolution as a function of MoN_x concentration in the bottom electrode.

Microstructural and interfacial imaging

The film microstructure was examined using a FE-SEM, and the grain size was analyzed by the watershed method in the Gwyddion software[37]. For cross-sectional analysis, electron microscopy specimens were prepared using a focused ion beam (FIB) system (Helios Nanolab 650, FEI, Netherlands). To protect the surface from ion-beam damage during milling, protective Pt and carbon layers were deposited on the region of interest. The prepared thin lamella was extracted using a standard lift-out technique and mounted onto a copper (Cu) grid.

Cross-sectional microstructures and atomic-scale elemental distributions were then analyzed using high-resolution transmission electron microscopy (HRTEM). High-resolution scanning transmission electron microscopy (HR-STEM) and energy-dispersive spectroscopy (EDS) were performed using a JEM-ARM200F microscope (JEOL Ltd., Japan) operated at 200 kV. Electron energy-loss spectroscopy (EELS) line scans were acquired to probe the chemical bonding states of N and O across the interface. To enhance signal intensity, the scans were performed with a fine step size of 0.2 nm, and the spectra were subsequently integrated over 2 nm intervals for analysis.

Statistical analysis

To ensure the statistical reliability of the reported data, rigorous statistical analyses were performed for both electrical and structural measurements. For evaluation of the ferroelectric properties (P_r and E_c), data were collected from 10 randomly selected, distinct capacitor devices for each electrode condition to account for device-to-device variation. For IL-thickness quantification, depth-dependent HRTEM intensity profiles were extracted and analyzed from five randomly selected locations for each sample. This approach accounts for local interfacial undulations and improves the statistical representativeness of the measurements. At each location, the local IL thickness was determined from the full width at half maximum (FWHM) of a Gaussian fit to the interfacial intensity peak. All statistically analyzed results are reported as average values with corresponding standard deviations to reflect data dispersion.

RESULTS AND DISCUSSION

As shown in the top panel of Figure 1A, elemental Mo adopts a body-centered cubic structure, whereas N incorporation stabilizes rock-salt-derived MoN_x phases. In this family, B1-MoN corresponds to full anion-site occupancy, while γ-Mo_2N can be viewed as an anion-vacancy derivative with partial anion-site occupancy. In this work, we systematically control the Mo:N ratio in sputtered MoN_x electrodes and investigate how electrode stoichiometry governs the interfacial microstructure and electrical performance of ferroelectric HZO capacitors.

This approach addresses limitations intrinsic to MoO_x electrodes. As the O content increases in MoO_x, MoO_3 can form. Because MoO_3 is semiconducting, it may introduce parasitic capacitance, generating depolarization fields, and/or degrade carrier-injection barriers at the Mo/HZO interface, thereby increasing leakage. In contrast, MoN_x generally maintains metallic behavior over a broad composition window, enabling stable use as a conductive electrode while providing an additional compositional knob for interfacial chemistry control.

Figure 1B shows Bragg-Brentano XRD patterns of four MoN_x films deposited by Ar/N_2 sputtering with controlled N_2/(Ar + N_2) flow ratios of 0%, 5%, 20%, and 50%. The corresponding compositions are x = 0.00, 0.05, 0.52, and 0.79, denoted as Mo, 05MoN, 52MoN, and 79MoN, respectively. The composition-extraction procedure is provided in Supplementary Figure 1 and Supplementary Table 1. Mo exhibits strong (110) preferred orientation. The low-N film (05MoN) shows very broad diffraction features, consistent with reduced crystallite size and/or mixed-phase character. Because both Mo and γ-Mo_2N are metallic, 05MoN is still expected to operate as an electrode. In contrast, 52MoN and 79MoN exhibit well-developed cubic rock-salt-type diffraction peaks with pronounced (111) preferred orientation, suggesting increased crystallographic compatibility with low-index HZO planes[38] [Figure 1C].

Figure 1D and E summarize resistivity and work function, respectively. Resistivity is lowest for elemental Mo and generally increases with N content. Importantly, even 52MoN, which shows the highest resistivity among the measured films, remains below ~ 200 μΩ·cm, which is sufficiently low for electrode operation.

The work function increases from 4.70 eV for Mo to 4.94 eV for 52MoN and then decreases to 4.76 eV for 79MoN. Although the bulk composition evolves monotonically toward the N-rich rock-salt MoN_x regime, the UPS-derived work function does not follow a simple linear trend with the average stoichiometry. Instead, the measured value is highly sensitive to the near-surface electronic structure. The reduced work function of 79MoN suggests that in the highly N-rich regime, surface-sensitive factors such as surface termination, local phase constitution, nitrogen-vacancy population, and residual surface oxidation play dominant roles in determining the effective work function. The UPS data are provided in Supplementary Figure 2.

Electrode microstructure was further examined by planar SEM and AFM. Grain-size distributions extracted from SEM images using Gwyddion [Supplementary Figure 3] yield average lateral grain radii of ~ 3.9-4.7 nm assuming cylindrical grains, with a modest increase as N content increases. AFM analysis confirms well-optimized sputtering conditions, showing that all electrodes exhibit smooth surfaces with root-mean-square roughness (R_q) values below 0.55 nm [Supplementary Figure 4].

After establishing the electrode series, symmetric MoN_x/HZO/MoN_x capacitors were fabricated by depositing 8 nm HZO by ALD, followed by sputtered top electrodes with the same MoN_x composition. To assess how electrode stoichiometry affects IL formation during ALD and subsequent crystallization annealing, cross-sectional STEM-EDS and STEM-EELS analyses were performed.

Figure 2A and B present cross-sectional high-magnification HRTEM images of the Mo/HZO/Mo and 52MoN/HZO/52MoN capacitor stacks, respectively. To quantitatively analyze the IL formed at the bottom interface, depth-dependent HRTEM intensity profiles were extracted from the indicated regions. The IL thickness was determined by calculating the FWHM from a Gaussian fit of the bright IL intensity peak located between the electrode and the HZO bulk. As supported by the statistical analysis [Figure 2C], the pure Mo stack exhibits a prominent IL with an average thickness of 2.20 ± 0.21 nm. In sharp contrast, the 52MoN stack in Figure 2B shows a significantly suppressed IL with an average thickness of only 1.15 ± 0.07 nm. This corresponds to a 47.7% reduction in IL thickness for 52MoN relative to the Mo electrode.

Figure 2D and E present STEM-EDS elemental maps for these stacks. In both stacks, an IL is observed at the bottom electrode/HZO interface, where oxygen signals overlap with electrode elements. The observed difference in thickness is consistent with the higher oxidation resistance of N-containing MoN_x under ozone exposure during ALD. In addition, N is detected within the HZO film in Figure 2E, indicating that N can incorporate into HZO, most plausibly during the post-deposition anneal given diffusion kinetics. Thermodynamically, the strong stability of nitrides such as HfN and ZrN relative to Mo_2N (formation free energies at 700 K: -638.8 and -595.6 $kJ \cdot mol^{-1}$ for HfN and ZrN, respectively, *vs.* -52.4 $kJ \cdot mol^{-1}$ for Mo_2N) provides a driving force for N transfer into the HZO interfacial region[39,40].

The EELS line-scan positions across the Mo/HZO/Mo stack are indicated in Figure 2F, and the corresponding O-K edge spectra are shown in Figure 2G. Similarly, the scan positions for the 52MoN/HZO/52MoN stack are presented in Figure 2H, with the corresponding N-K and O-K edge spectra displayed in Figure 2I and J, respectively. The line-scan colors match the indicated positions. Within HZO, the O-K edge exhibits the expected double-peak features in the 532-533 eV and 536-537 eV ranges [Figure 2G and J]. Ideally, if the electrodes remain unoxidized, no O-K peak would be observed in the electrode region. However, in Mo/HZO/Mo (green circles in Figure 2G), both the top and bottom Mo electrodes exhibit an O-K feature near ~ 532 eV, indicating electrode oxidation and the presence of a MoO_x IL[41]. Stoichiometric MoO_3 typically exhibits a clearly separated doublet, whereas oxygen-deficient MoO_x tends to show less distinct splitting. Therefore, the observed interfacial oxide is more consistent with oxygen-deficient MoO_x than with fully stoichiometric MoO_3. This structurally defective and relatively less dense

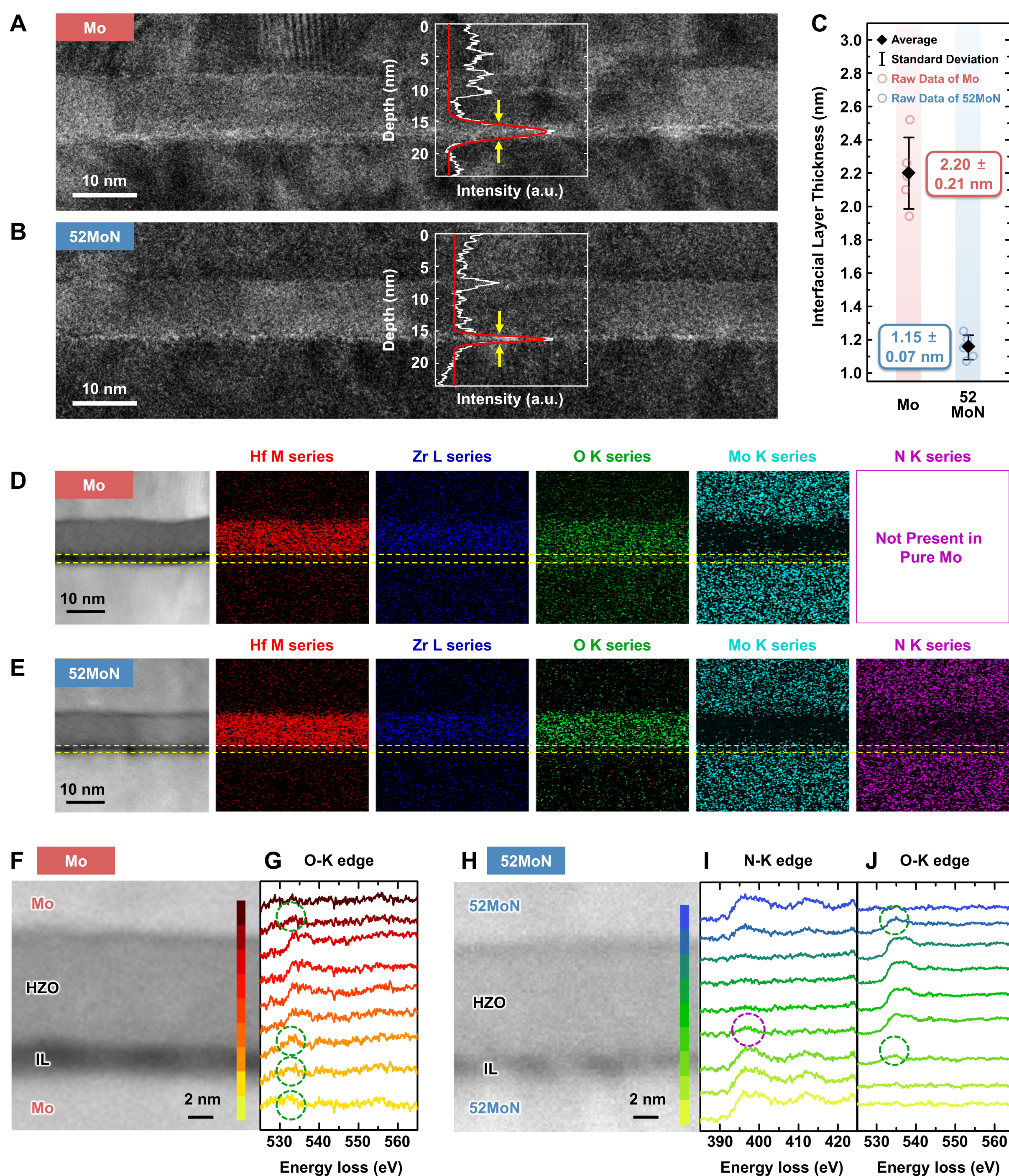

Figure 2. Microstructural and chemical analysis of electrode/HZO interfaces. Cross-sectional HRTEM images of the (A) Mo- and (B) 52MoN-based capacitors, respectively. These high-resolution images were used for precise IL thickness quantification to address the spatial resolution limitations of chemical mapping. The inset graphs in Figure 2A and B show representative depth-dependent HRTEM intensity profiles obtained by horizontal box-averaging; (C) Statistical analysis of the IL thicknesses extracted from 5 randomly selected regions across the full-span HRTEM images (see Supplementary Figure 5 for details). Based on this statistical extraction, the average IL thicknesses, determined by Gaussian fitting (FWHM), were estimated as 2.20 ± 0.21 nm for the Mo stack and 1.15 ± 0.07 nm for the 52MoN stack. Scanning transmission electron microscopy-energy-dispersive spectroscopy (STEM-EDS) elemental maps for the (D) pure Mo and (E) 52MoN stacks, showing Hf, Zr, O, Mo, and N distributions. The N map of the pure Mo stack is marked as 'Not Present in Pure Mo' because no nitrogen was introduced during the sputtering process of the pure Mo electrode. (F-J) EELS analysis; (F and G) show the HAADF image and O-K edge spectra for pure Mo, and H-J show the HAADF image, N-K edge, and O-K edge spectra for 52MoN, respectively. In Figure 2G, the green dashed circles mark the O-K edge features in the Mo electrode region, which signify interfacial Mo oxidation. In Figure 2I, the purple dashed circle marks the weak N-K edge signal within the HZO side near the bottom interface, providing evidence of nitrogen incorporation. In Figure 2J, the green dashed circles indicate the restricted O-K edge signals adjacent to the interfaces, thereby confirming the suppressed oxidation in the 52MoN stack. Line-scan colors correspond to the positions indicated in the HAADF images. IL: Interfacial layer; HZO: $Hf_{0.5}Zr_{0.5}O_2$; HRTEM; high-resolution transmission electron microscopy; FWHM: full width at half maximum; EELS: electron energy-loss spectroscopy. HAADF: high-angle annular dark-field.

oxygen-deficient MoO_x layer is consistent with the bright contrast observed in the HRTEM images, because it permits higher electron transmission than the adjacent dense Mo and HZO layers. Notably, the bottom interface shows O-K peaks in the three spectra closest to the interface (green circles in Figure 2G). If the line-scan spacing is ~ 2 nm, this corresponds to an oxide thickness of approximately 4-6 nm. This chemical oxygen-penetration depth is larger than the structural IL thickness (~ 2.20 nm) observed by HRTEM. While HRTEM visualizes the severely amorphized, structurally defective region through contrast variation, the EELS captures deeper oxygen diffusion that forms an oxygen-deficient MoO_x layer without completely collapsing the underlying Mo crystalline lattice. In contrast, the top Mo electrode shows an O-K peak in only one spectrum, implying weaker oxidation. This asymmetry indicates that Mo oxidation likely occurs predominantly during the highly reactive ozone pulses used in the initial ALD growth of HZO on the bottom electrode at 280 °C, rather than during the subsequent RTP step, consistent with earlier observations in Mo-based HZO stacks.

A markedly different behavior is observed for 52MoN/HZO/52MoN. In Figure 2I, a strong N-K peak appears near ~ 398 eV within the 52MoN electrode region, consistent with typical transition-metal nitride signatures (~ 397-400 eV)[42]. Importantly, a weak N-K signal is also detected within HZO near the bottom interface (purple circle in Figure 2I), directly evidencing partial N incorporation into the HZO interfacial region. Moreover, the O-K line-scan analysis [Figure 2J] shows that electrode oxidation is strongly suppressed: only the spectra immediately adjacent to the interfaces exhibit an O-K peak, indicating that the oxidized region is confined to a much thinner interfacial zone than in Mo/HZO/Mo. Together, these results experimentally confirm that higher N content in MoN_x significantly mitigates ALD-induced bottom-electrode oxidation and reduces defective IL formation.

To elucidate the origins of the electrical differences and isolate bottom-interface reactions, interfacial chemistry and O transport were examined using ToF-SIMS and XPS [Figure 3A and B]. Simplified stacks consisting of 8 or 2.5 nm HZO deposited on Mo or MoN_x were fabricated to focus on the bottom interface.

The ToF-SIMS depth profiles reveal a clear contrast between the Mo and MoN_x series. In these profiles, the shaded interfacial boundaries are schematically highlighted as a visual guide to indicate the chemical transition zone, encompassing the broad peak distribution of the HfO_2^- secondary ion signal, which acts as a chemical marker due to the matrix effect[44]. In the Mo reference sample, O penetrates deeply into the electrode during HZO growth and subsequent annealing, forming a relatively thick oxide interfacial region and an extended MoO_x zone associated with strong interfacial damage (red circle in Figure 3A). Notably, the low-N 05MoN electrode exhibits an even thicker oxide IL despite N incorporation. This result indicates that introducing only a small amount of N can degrade Mo crystallinity and facilitate deep O penetration. At higher N contents, the behavior changes qualitatively: 52MoN and 79MoN show pronounced N accumulation near the interface and within the HZO side (green circles in Figure 3A), suggesting that a nitride-rich interfacial region functions as a barrier against excessive oxidation.

These coupled O/N transport processes are further supported by XPS [Figure 3B]. Upon annealing, the Mo 3d spectra show the reduction of MoO_3 toward MoO_2 (red arrows in Figure 3B) and a concurrent shift of the Mo-N component toward a higher binding energy. These results imply that MoO_3 can act as an oxygen reservoir supplying O to both HZO and the underlying electrode, while N in MoN_x diffuses into the interfacial region of HZO and modifies local bonding configurations. The observed chemical-state evolution is consistent with the Gibbs free-energy hierarchy shown in Figure 3C and D. Figure 3E summarizes the maximum secondary-ion intensities of MoO^-, MoO_2^-, and HfN^- fragments extracted from the ToF-SIMS profiles. Collectively, these data indicate that N incorporation is established predominantly during HZO ALD and/or early thermal steps, whereas annealing primarily redistributes V_os rather than contributing to

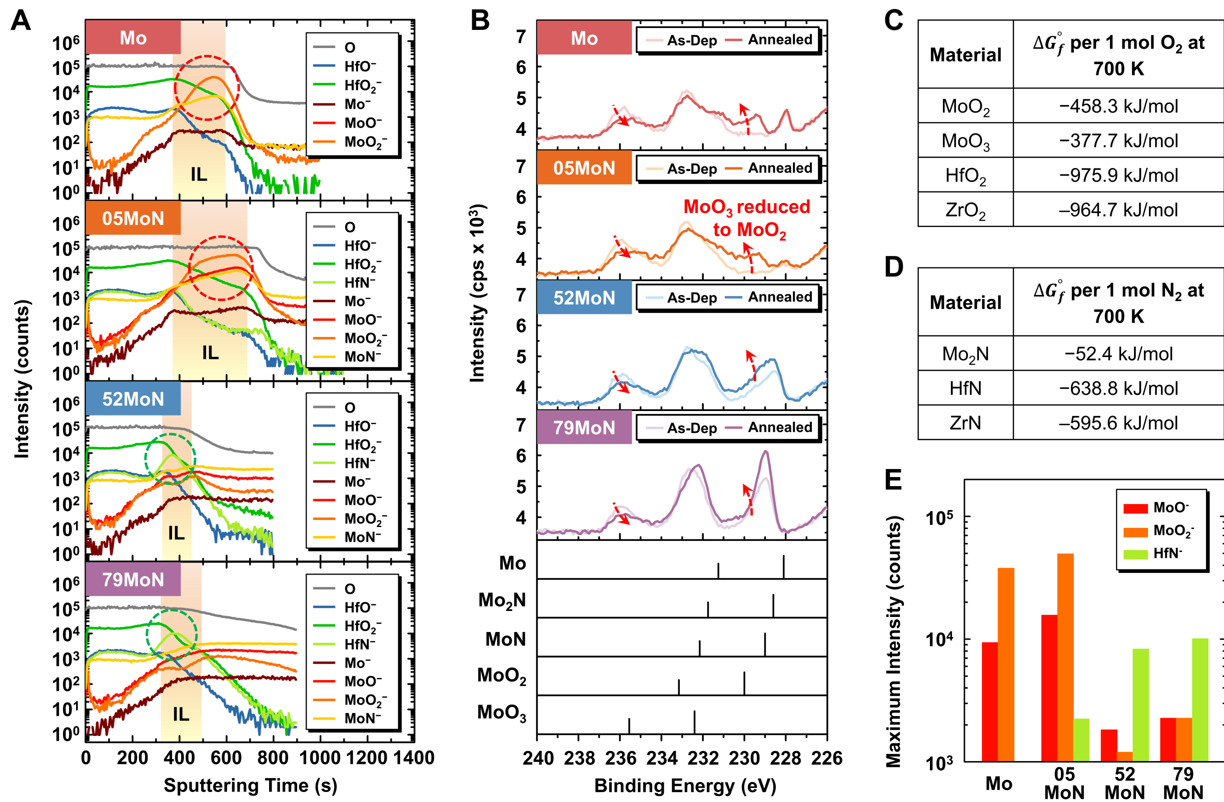

Figure 3. Analysis of interfacial chemical composition and thermodynamic stability. (A) Time-of-flight secondary ion mass spectrometry (ToF-SIMS) depth profiles were obtained from HZO/MoN_x stacks with pure Mo, 05MoN, 52MoN, and 79MoN bottom electrodes. The profiles highlight the elemental distribution across the interfacial layer. The shaded areas are schematically highlighted as visual guides to denote the interfacial chemical transition zones, roughly encompassing the peak regions of the HfO_2- secondary ion signals. The red dashed circles mark the significant accumulation of oxygen-related fragments (MoO^- and MoO_2^-) within the IL for the Mo and 05MoN stacks, indicating severe oxidation. Conversely, the green dashed circles mark the peak of nitrogen-related fragments (HfN-) in the 52MoN and 79MoN stacks, indicating a nitride-rich interfacial region; (B) The evolution of Mo 3d X-ray photoelectron spectroscopy spectra was analyzed for as-deposited and annealed HZO/MoN_x stacks, showing the reduction of higher-valence oxides upon annealing. The red arrows indicate the binding-energy shift associated with reduction of MoO_3 to MoO_2 upon annealing; (C) Standard Gibbs free energies of formation (ΔGf°) per 1 mol of O_2 at 700 K for relevant oxides[39,40]; (D) ΔGf° values per 1 mol of N_2 at 700 K for relevant nitrides[39,43]; (E) Maximum secondary-ion intensities of MoO^-, MoO^{2-}, and HfN^- fragments were extracted from the ToF-SIMS profiles.

substantial additional N diffusion.

Figure 4A shows GIXRD patterns of 8 nm HZO films crystallized on Mo, 05MoN, 52MoN, and 79MoN electrodes. For these measurements, MoN_x/HZO/MoN_x stacks were annealed, and the top electrode was removed by wet etching to avoid top-electrode contributions. Electrode diffraction peaks such as 110_{Mo} and 111_{MoN} are observed across samples, consistent with the Bragg-Brentano XRD patterns in Figure 1C.

HZO diffraction peaks are denoted as hkl_x, where x indicates the orthorhombic (O, $Pca2_1$), tetragonal (T, $P4_2/nmc$), or monoclinic (M, $P2_1/c$) phase. In all samples, a dominant peak near 30.5° 2θ is observed, corresponding to overlapping $111_O/101_T$ reflections. However, HZO films on Mo and 05MoN show clear monoclinic peaks at ~ 28.5° and ~ 31.7° (-111_M and 111_M). Peak deconvolution of the 27°-33° region [Supplementary Figure 6] enables estimation of the M phase fraction [Figure 4B]. The M phase fraction decreases systematically with N content: Mo yields the highest M phase fraction (~ 21%), whereas 52MoN and 79MoN reduce the M phase fraction to < 5%.

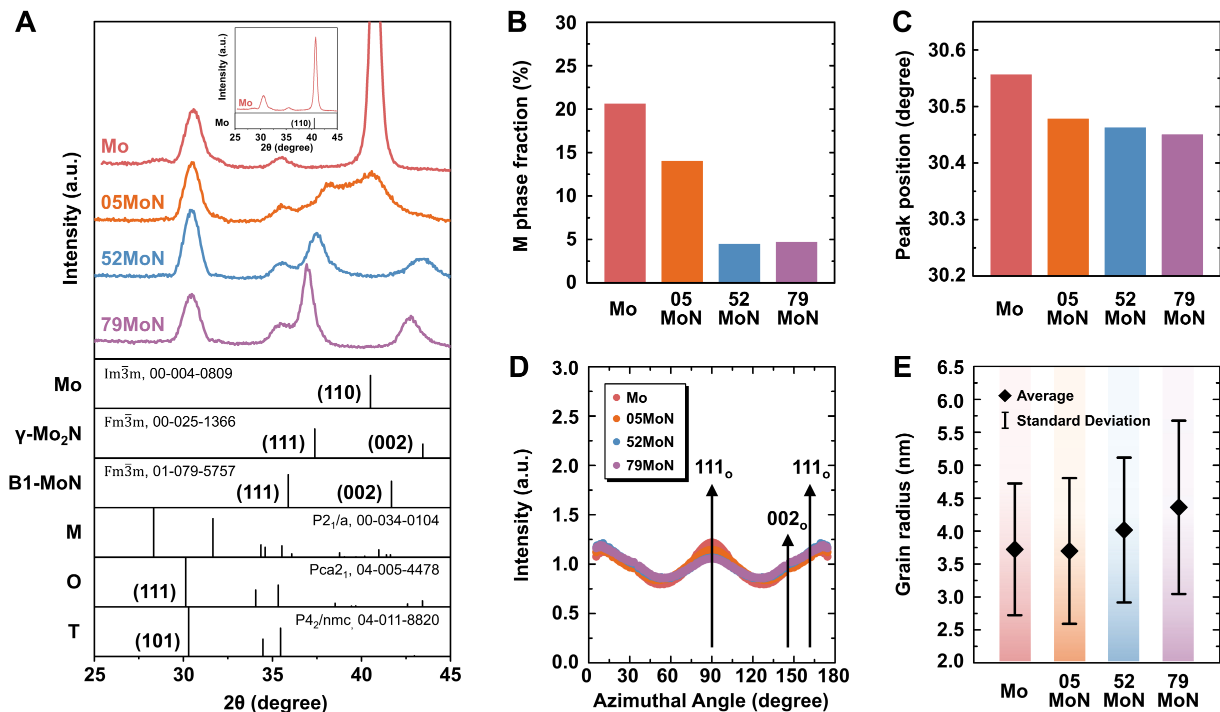

Figure 4. Crystallographic structural analysis of HZO thin films. (A) Grazing-incidence X-ray diffraction patterns obtained from HZO thin films deposited on Mo and MoN_x electrodes, along with reference patterns for Mo, molybdenum nitrides, and HZO polymorphs. The inset shows the full-intensity-scale pattern for the Mo electrode condition, illustrating the complete height of the Mo (110) peak. Structural parameters extracted from the XRD profiles, including (B) the monoclinic (M) phase fraction and (C) the 2θ position of the orthorhombic/tetragonal (O/T) peak near 30.5°; (D) Azimuthal intensity profiles of the orthorhombic 111 (111_O) and 002 (002_O) reflections were derived from grazing-incidence wide-angle X-ray scattering analysis. Data within the missing-wedge region were obtained by extrapolation using a Gaussian function; (E) Average grain radius determined for HZO films under each electrode condition. HZO: $Hf_{0.5}Zr_{0.5}O_2$.

Quantitative separation of the T phase and O phase fractions by conventional XRD is challenging because these structures are similar and their peaks overlap. Nevertheless, because the T phase peak is typically located near 30.8°[45,46] and the O phase peak near 30.4°[38, 47], the position of the combined $111_O/101_T$ peak can provide insight into their relative contributions. As N content increases, the peak position shifts from ~ 30.55° for Mo to ~ 30.45° for 79MoN [Figure 4C]. Although this shift toward lower angles suggests a tendency to favor orthorhombic contribution, it may also be influenced by residual strain arising from lattice expansion in the underlying MoN_x electrodes. Therefore, rather than indicating a large increase in the orthorhombic phase alone, these results suggest that higher-N MoN_x electrodes effectively suppress the non-ferroelectric monoclinic phase and stabilize an overall ferroelectric-compatible structural configuration. This interpretation is consistent with the stable double remanent polarization ($2P_r$) behavior observed in Figure 5 and the mitigated wake-up effect observed in the electrical measurements.

Because the HZO 002_O reflection overlaps with the diffraction signals from the MoN_x electrodes [Supplementary Figure 7], the texture analysis focused on the $111_O/101_T$ region. Figure 4D shows azimuthal cuts of the GIWAXS intensity around this peak, as indicated by the red dashed arcs in Supplementary Figure 7. An azimuthal angle of 90° corresponds to the substrate normal, whereas 0° and 180° correspond to in-plane directions. Although GIWAXS has limited access to the exact substrate-normal region, the 90° intensity was reconstructed by extrapolation, consistent with prior approaches. Overall, strong preferential orientation is not observed for HZO on any MoN_x electrode; if anything, the 111 fiber texture slightly decreases with increasing N content. TEM diffraction analyses [Supplementary Figure 8] likewise do not show strong texture.

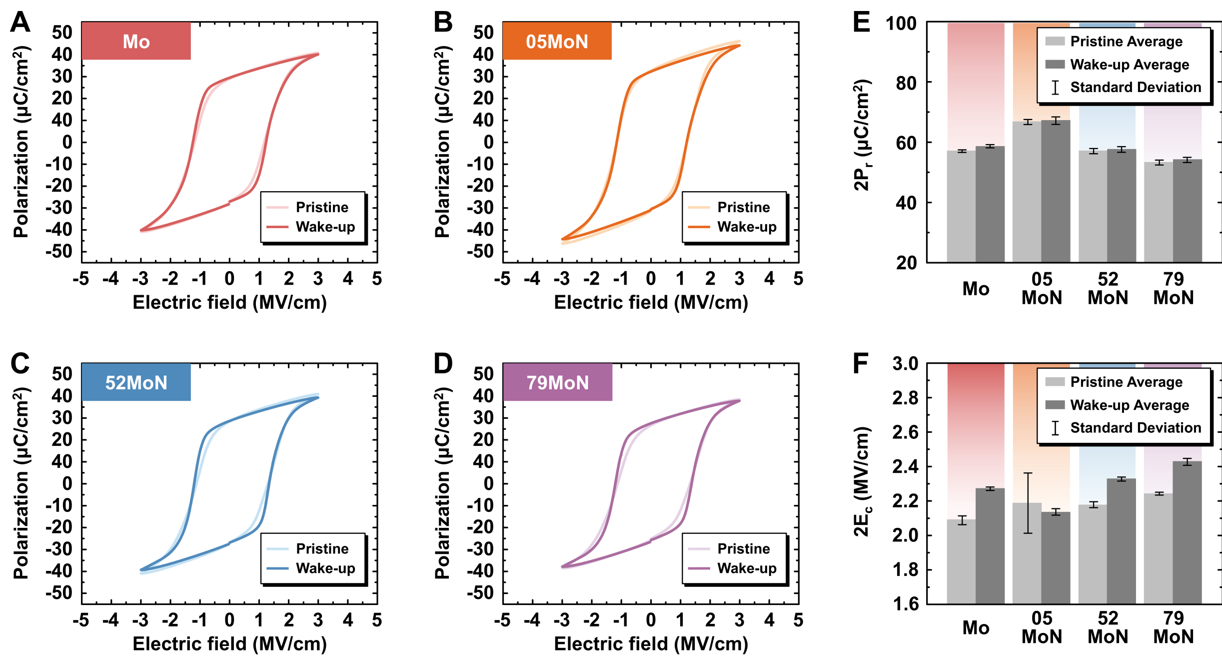

Figure 5. Ferroelectric switching characteristics and wake-up stability of HZO capacitors. P-E hysteresis loops were measured for HZO capacitors with (A) Mo, (B) 05MoN, (C) 52MoN, and (D) 79MoN electrodes. The loops compare the ferroelectric response in the pristine state and after wake-up field cycling (10^4 cycles at 3 MV•cm^{-1} and 100 kHz). The evolution of ferroelectric parameters is summarized in (E) Double remanent polarization ($2P_r$) and (F) double coercive field ($2E_c$), for each electrode condition before and after cycling. HZO: $Hf_{0.5}Zr_{0.5}O_2$; P-E: polarization-electric field.

Figure 4E summarizes the lateral grain-size analysis for HZO on MoN_x, extracted from planar SEM images using the watershed method in the Gwyddion software [Supplementary Figure 9]. The mean lateral grain radius (assuming cylindrical grains) shows a modest increase with N content but remains within ~ 3.8-4.4 nm. AFM topography of HZO [Supplementary Figure 10] reveals R_q below 0.65 nm for all films, indicating that MoN_x stoichiometry does not introduce significant roughening or morphological instability in the HZO layer.

Figure 5A-D show P-E hysteresis loops of Mo/HZO/Mo, 05MoN/HZO/05MoN, 52MoN/HZO/52MoN, and 79MoN/HZO/79MoN capacitors in the pristine state and after wake-up cycling. Wake-up cycling was performed at 3 MV·cm^{-1} and 100 kHz, for 10^4 cycles. Extracted $2P_r$ and double coercive field ($2E_c$) values are summarized in Figure 5E and F, respectively; additional P-E loops measured at various fields are provided in Supplementary Figures 11 and 12. To ensure statistical reliability and account for device-to-device variation (DTDV), ferroelectric parameters were extracted from 10 randomly selected devices for each condition. As summarized in Figure 5E, the average pristine $2P_r$ values are 57.02 ± 0.41, 66.69 ± 0.80, 57.02 ± 0.83, and 53.23 ± 0.78 μC·cm^{-2} for Mo, 05MoN, 52MoN, and 79MoN, respectively. After wake-up cycling, the corresponding average values are 58.66 ± 0.51, 67.13 ± 1.19, 57.56 ± 0.89, and 54.10 ± 0.84 μC·cm^{-2}. These statistical averages demonstrate that the relative $2P_r$ change upon wake-up remains exceptionally low (≤ 3.0%) across all optimized MoN_x stacks, confirming that the near-wake-up-free behavior is a robust intrinsic property rather than a measurement artifact.

A localized statistical anomaly is observed in the $2E_c$ of the pristine 05MoN stack [Figure 5F]. Although the $2P_r$ values remain statistically stable, pristine 05MoN capacitors exhibit a considerably larger standard deviation in $2E_c$ than the other conditions. This wide DTDV directly reflects the microstructural degradation observed in the chemical analyses [Figures 1 and 3]. The low-N 05MoN film has a mixed-phase character with degraded crystallinity, which facilitates severe and non-uniform oxygen penetration during ALD and

forms a highly defective, thick MoO_x interfacial layer. Unlike $2P_r$, which is primarily governed by the volume-averaged phase fraction, $2E_c$ is highly sensitive to localized pinning sites and interfacial defect distributions. The structurally non-uniform interface therefore introduces substantial local variation in the initial defect distribution, leading to a broad distribution of switching barriers across devices. After wake-up cycling, the electric-field-driven redistribution and stabilization of these interfacial defects effectively homogenize the switching paths, resulting in a noticeably narrower $2E_c$ variance. Moreover, the change in $2E_c$ is limited to ≤ 8.0% across all stacks [Figure 5F], indicating a stable switching barrier and a consistent ferroelectric response with minimal electrical conditioning. This near-wake-up-free behavior is attractive for ferroelectric memory applications because it reduces variability and eliminates the need for extensive post-fabrication field training.

Figure 6A-C show the evolution of $2P_r$ under bipolar cycling at 2.4, 2.0, and 1.6 V (100 kHz). Figure 6D-F summarize the evolution of $2E_c$ and imprint field [$E_{imp} = (E_c^+ + E_c^-)/2$]. Endurance strongly depends on electrode N content. At 2.4 V, the highest field condition, Mo and low-N MoN_x (05MoN, corresponding to 5% N_2 flow) exhibit relatively early breakdown near ~ 10^5 cycles, whereas higher-N electrodes (52MoN and 79MoN, corresponding to 20% and 50% N_2 flow) maintain stable switching up to ~ 10^6 cycles [Figure 6A]. In this high-field regime, the increase in polarization during the initial 10^4 cycles is only ~ 0.20-1.70 μC·cm^{-2} (≤ 3.1%) for all electrodes, consistent with strongly suppressed wake-up.

Reducing the cycling voltage to 2.0 V expands the endurance window by roughly two orders of magnitude [Figure 6B]: Mo and 05MoN fail near ~ 10^6 cycles, 52MoN remains switchable to ~ 10^7 cycles, and 79MoN sustains cycling to ~ 10^8 cycles. Under this condition, Mo, 05MoN, and 52MoN retain more than ~ 68% of their initial polarization at their respective maximum cycle counts. In contrast, 79MoN shows a stronger reduction in apparent polarization to approximately one-third of its initial value by 10^8 cycles, consistent with its higher coercive field and increasingly incomplete switching at 2.0 V. At 1.6 V, the applied voltage is below $2E_c$ for all capacitor stacks [Figure 6F]. Therefore, the extracted polarization corresponds to partial or minor-loop switching, and the decrease in $2P_r$ under this condition should be attributed mainly to incomplete polarization reversal rather than catastrophic dielectric breakdown. Nevertheless, the capacitors sustain very high cycle counts: Mo, 05MoN, and 52MoN remain functional to at least ~ 10^8 cycles, and 79MoN endures up to ~ 10^9 cycles. In this sense, the 1.6 V result represents a low-voltage survival window, whereas the 2.0 V data are more representative of practical switching endurance. Overall, 79MoN provides the longest endurance but at the cost of reduced apparent polarization under limited-voltage operation, whereas 52MoN maintains higher polarization with excellent cycling stability. Thus, 52MoN is the most favorable compromise between polarization and endurance for practical operation.

The central outcome of this work is that MoN_x stoichiometry provides a single-layer lever for controlling the interfacial microstructure that governs ferroelectric HZO performance. By systematically varying N content, we simultaneously tune (i) oxidation resistance and O permeability of the bottom electrode during ozone-based ALD and (ii) N availability for interfacial incorporation into HZO. This coupled chemical and microstructural control directly translates into phase stabilization, wake-up suppression, and improved cycling reliability.

STEM-EDS/EELS and ToF-SIMS consistently show that oxygen penetrates deeply into Mo during HZO ALD and annealing, forming a thick MoO_x region associated with interfacial damage. Increasing N content dramatically confines this oxidation to a thinner region, culminating in the high-N electrodes (52MoN and 79MoN), for which O-K edge signals in the electrode appear only in the spectra closest to the interface. This behavior indicates that N-rich MoN_x effectively acts as a redox/transport barrier under ALD conditions.

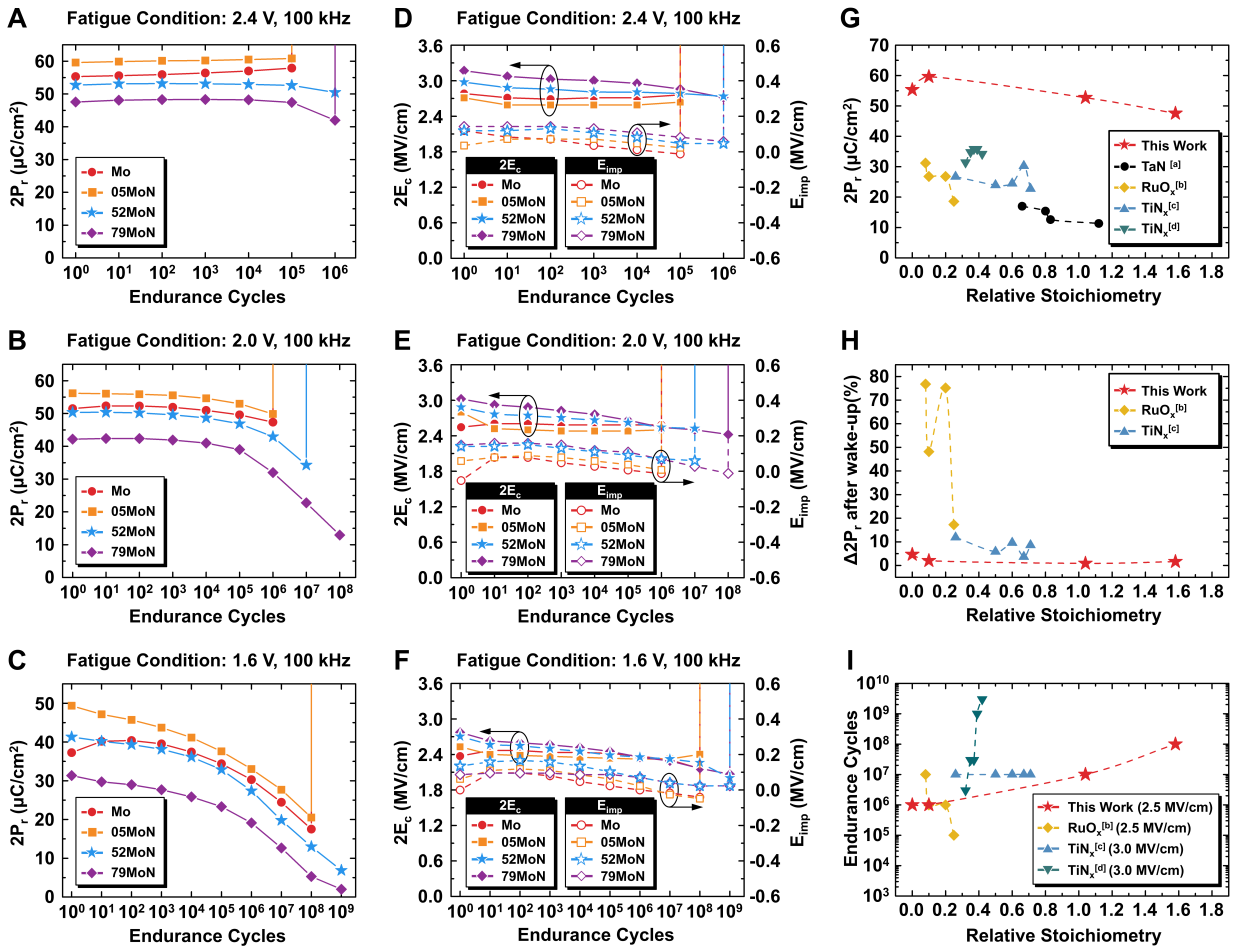

Figure 6. Endurance cycling characteristics of HZO capacitors. Endurance characteristics were evaluated for HZO capacitors with Mo and MoN_x electrodes using bipolar rectangular pulses at 100 kHz. The evolution of (A-C) $2P_r$ and (D-F) $2E_c$ and imprint field [E_{imp} = (E_c^+ + E_c^-)/2] was monitored as a function of switching cycles. In (D-F), solid symbols represent $2E_c$ plotted on the left y-axis, whereas hollow symbols denote E_{imp} plotted on the right y-axis. The black arrowed circles in D-F highlight representative $2E_c$ (left-pointing arrows) and E_{imp} (right-pointing arrows) data to clarify their corresponding y-axes. The data were obtained under applied voltages of 2.4 V (A and D), 2.0 V (B and E), and 1.6 V (C and F); (G-I) Benchmark comparison of ferroelectric properties with other stoichiometrically controlled electrode systems, including TaN_x[a], RuO_x[b], and TiN_x[c,d]. (G) Pristine-state $2P_r$ values and (H) percentage change in $2P_r$ after wake-up ($\Delta 2P_r$) plotted against relative stoichiometry. For this work, data were extracted from Figure 6A, where $\Delta 2P_r$ is defined as [($2P_{r,\,max}$ - $2P_{r,\,pristine}$)/$2P_{r,\,pristine}$] × 100%. Comparative data were obtained under electric fields of 2.5 MV•cm^{-1} for TaN_x and RuO_x and 3.0 MV•cm^{-1} for this work and TiN_x. (I) Benchmark comparison of endurance cycles plotted against relative stoichiometry. Endurance data for this work and RuO_x[b] were obtained under an electric field of 2.5 MV•cm^{-1}, whereas data for TiN_x[c,d] were evaluated at 3.0 MV•cm^{-1}. References [a]-[d] correspond to references[48-51], respectively. HZO: $Hf_{0.5}Zr_{0.5}O_2$.

A particularly important and practically relevant observation is that low-N MoN_x (05MoN) can form an even thicker oxidized IL than pure Mo. This result implies that oxidation resistance cannot be inferred solely from the presence of N; rather, insufficient N may degrade crystallinity and open fast diffusion pathways, thereby facilitating O penetration. Thus, MoN_x does not follow a simple monotonic trend, and a threshold N content is required to form a stable, oxidation-resistant, nitride-rich interfacial microstructure.

In high-N stacks, a weak but measurable N-K signal appears within HZO near the bottom interface, and ToF-SIMS shows nitride-related fragments on the HZO side. These results support a scenario in which MoN_x supplies N to the interfacial HZO region during ALD and/or annealing. Because V_os in HZO are widely associated with deep traps that can facilitate Poole-Frenkel conduction and trap-assisted tunneling[52], N incorporation provides a plausible pathway for V_o compensation and trap-state modification. Furthermore

, steady-state leakage-current measurements [Supplementary Figure 13] reveal that the pristine macroscopic leakage levels remain comparable across the electrode variations. This indicates that the dramatic enhancement in cycling stability is not driven by a reduction in initial global leakage but rather by the suppression of localized leakage-current paths during prolonged electric-field cycling[52,53]. Although direct trap spectroscopy is outside the present scope, the concurrent suppression of defective MoO_x growth, which typically acts as a vulnerable reservoir for defect clustering, together with evidence of N incorporation, provides a coherent microstructure-based explanation for the inhibition of defect-mediated percolation paths and the resulting reliability improvements observed in endurance tests.

GIXRD reveals that increasing N content strongly suppresses the monoclinic fraction, from ~ 21% on Mo to < 5% on 52MoN/79MoN, while the 30.5° peak position shifts in a manner consistent with an increased orthorhombic contribution. This structural evolution aligns with the electrical signature of near-wake-up-free switching (≤ 3.0% change in $2P_r$ after 10^4 cycles). In conventional TiN-electrode HZO, wake-up is often attributed to field-driven redistribution of V_os and gradual conversion of non-ferroelectric regions into ferroelectric domains. Here, the small wake-up indicates that the as-fabricated stacks already possess a more favorable defect/phase configuration, consistent with reduced interfacial oxidation and modified O/N chemistry.

To further validate the advantages of the MoN_x system, we benchmarked its ferroelectric properties and reliability against other reported stoichiometry-controlled electrode materials, including TaN_x, RuO_x, and TiN_x [Figure 6G-I]. As shown in Figure 6G, MoN_x-based capacitors exhibit high pristine $2P_r$ values exceeding 47.5 μC·cm^{-2} across the entire investigated stoichiometric range, outperforming the comparative systems, which generally show lower polarization or stronger composition dependence. Figure 6H further highlights the wake-up immunity of our devices. While other material systems often show substantial wake-up, with up to a 76.8% increase in $2P_r$ after cycling, the MoN_x electrodes maintain negligible polarization changes regardless of N content. We acknowledge that some prior studies on HZO-based capacitors have reported superior absolute endurance values exceeding 10^{11} cycles under highly optimized device and testing conditions[5,11,54]. However, when benchmarking specifically against variable-stoichiometry systems such as TiN_x and RuO_x, as illustrated in Figure 6I, high reliability is often highly sensitive to stoichiometric variations; even slight deviations can lead to a drastic reduction in cycle life. In contrast, the MoN_x platform provides a broader and more robust reliability window, enabling predictable endurance enhancement across a wide compositional range. Moreover, because endurance is known to degrade exponentially as HZO thickness is scaled down, achieving stable operation up to 10^8-10^9 cycles in an 8 nm thin film is significant. This comparison underscores that the MoN_x platform offers an optimal balance of robust ferroelectricity, immediate reliability, and sustained cycle life, thereby mitigating the trade-offs commonly observed in other variable-stoichiometry electrodes.

Beyond the immediate performance improvements, MoN_x is attractive because it enables interfacial engineering without multilayer electrode stacks, which can complicate thickness scaling and introduce additional series resistance. Future work can expand this platform by correlating IL-thickness distributions with breakdown statistics, directly probing trap spectra, and exploring process variables such as N content, deposition temperature, and surface termination to tune E_c without sacrificing oxidation resistance. The ability to modulate stoichiometry over a wide range while maintaining weak oxygen-scavenging behavior is an intrinsic advantage of MoN_x compared with other transition-metal compounds examined to date. TiN and TaN can also retain rock-salt structures over broad stoichiometric ranges; however, their interfacial redox chemistry is strongly affected by the oxygen-scavenging nature of the metal constituents because of strong metal-oxygen bonding. Although hexagonal MoN is thermodynamically more stable than the B1-MoN phase, this work shows that B1-type MoN_x can be reliably formed in thin-film form suitable for

semiconductor electrode applications despite its metastability.

Although this study demonstrates the excellent interfacial stability of MoN_x electrodes using an 8 nm HZO model system, dielectric-thickness scaling introduces more severe challenges, including enhanced depolarization fields and direct tunneling currents. To explore this scaling behavior, we evaluated the ferroelectric properties of capacitors with HZO thickness scaled down to 6 nm [Supplementary Figure 14]. The ferroelectric response remains observable at 6 nm, but the hysteresis loops exhibit significant rounding, indicating that macroscopic leakage begins to dominate the electrical response. In such ultrathin regimes, suppression of the defective MoO_x interfacial layer by MoN_x is expected to be even more critical for maintaining acceptable leakage levels. However, at scaled thicknesses of ≤ 5 nm, macroscopic leakage currents heavily dominate the response, and intrinsic ferroelectric switching becomes completely masked, making it difficult to reliably decouple the purely interfacial benefits of the electrode. Process conditions such as annealing temperature and oxidant dose are also expected to strongly influence the delicate balance between bulk HZO crystallization and interfacial oxidation. For example, more aggressive oxidation conditions would likely exacerbate the degradation of elemental Mo and further necessitate the robust barrier properties of MoN_x. Therefore, future studies focused on co-optimizing these thermal and chemical parameters will be essential to fully unlock the potential of MoN_x electrodes for ultrathin (≤ 5 nm) ferroelectric memory applications.

CONCLUSIONS

In summary, we demonstrated that stoichiometry-tunable MoN_x can serve as a scalable single-layer electrode platform for ALD-grown ferroelectric HZO, enabling deterministic control of interfacial chemistry and device reliability. By sputter-depositing MoN_x electrodes with x = 0.00, 0.05, 0.52, and 0.79 and integrating them into symmetric MoN_x/HZO/MoN_x capacitors, we established a clear composition-microstructure-property relationship. Structural characterization confirmed that increasing N content drives the electrode toward a rock-salt-type MoN_x phase with (111) texture while retaining electrode-grade conductivity.

Importantly, we elucidated the role of nitrogen incorporation in modifying the interfacial redox dynamics during the aggressive ozone-based ALD process. N-rich MoN_x electrodes function as robust transport barriers, markedly suppressing ALD-induced electrode oxidation and confining the defective oxide layer to a thin interfacial zone. This controlled stoichiometry also facilitates partial nitrogen incorporation into the HZO layer near the bottom interface. The resulting interfacial chemistry provides crystallographic benefits by stabilizing a ferroelectric-compatible structure and significantly suppressing non-ferroelectric M phase formation without requiring complex multilayer electrode engineering.

From an electrical perspective, this microstructural optimization directly addresses critical reliability bottlenecks in HZO-based devices. The fabricated MoN_x stacks exhibit near-wake-up-free switching and extended endurance stability across a broad compositional window, distinguishing this platform from conventional variable-stoichiometry electrodes. In particular, 52MoN is identified as a best-balanced composition that combines strong oxidation resistance, minimized wake-up, robust polarization, and excellent cycling stability. Overall, this work shows that composition-engineerable MoN_x electrodes provide a versatile and scalable pathway for interfacial defect and redox engineering, advancing the viability of high-performance ferroelectric memory technologies.

DECLARATIONS

Acknowledgments

The authors thank Prof. Cheol Seong Hwang at Seoul National University for providing access to the four-point probe and XRF instrumentation. XPS, UPS, ToF-SIMS, SEM, FIB, and HR-STEM measurements

were carried out at the National Center for Inter-university Research Facilities (NCIRF). The authors also acknowledge the Research Institute of Advanced Materials (RIAM) for access to AFM, XRD, and GIXRD facilities and thank the staff at RIAM and NCIRF for their continued support in operating and maintaining these facilities.

Authors' contributions

Made substantial contributions to the conception and design of the study, acquisition, formal analysis, and interpretation of the data, and drafted the original manuscript: Choi, H.
Contributed to the acquisition of data, interpretation of the results, and participated in the critical revision of the manuscript: Park, J. Y.; Lee, J.; Jeong, H. W.; Yang, K.; Lee, S. Y.; Han, D. I.; Hong, H.
Contributed to the acquisition and formal analysis of the data and substantially contributed to the revision of the manuscript: Kim, Y. Y.
Contributed to the conceptualization, data analysis, and interpretation; critically revised the manuscript for important intellectual content; and provided administrative, technical, and material support for the project: Park, M. H.

Availability of data and materials

The original contributions presented in this study are included in the article and Supplementary Materials. Further inquiries can be directed to the corresponding author.

AI and AI-assisted tools statement

During the preparation and language revision of this manuscript, the authors used AI-assisted language tools, including Gemini 3.1 Pro (Google) and ChatGPT 5.5 Pro (OpenAI), solely to improve readability, check grammar, and polish the language of the text. After using these tools, the authors carefully reviewed and edited the content as needed. The authors take full responsibility for the final content of the publication. The authors confirm that no AI or AI-assisted technologies were used to alter data, interpret results, or generate any figures or graphical elements, thereby preserving the strict originality of the scientific findings.

Financial support and sponsorship

This work was supported by the National Research Foundation of Korea (RS-2025-13532975 and RS-2024-00441473). The aforementioned NRF grant (RS-2024-00441473) is supported under the collaborative framework of the CHIP JU project (ViTFOX, GA No. 101194368). Experiments at PLS-II were supported in part by the Korean government (MSIT) and Pohang University of Science and Technology.

Conflicts of interest

The authors declare no conflict of interest.

Ethical approval and consent to participate

Not applicable.

Consent for publication

Not applicable.

Copyright

© The Author(s) 2026.

Supplementary Materials

Supplementary Materials

REFERENCES

1. Böscke, T. S.; Müller, J.; Bräuhaus, D.; Schröder, U.; Böttger, U. Ferroelectricity in hafnium oxide thin films. *Appl. Phys. Lett.* **2011**, *99*, 102903. DOI

2. Lee, M.; Kim, J.; Le, D. N.; et al. BEOL compatible ultra-low operating voltage (0.5 V) and preconfigured switching polarization states in effective 3 nm ferroelectric HZO capacitors. In *2024 IEEE Symposium on VLSI Technology and Circuits (VLSI Technology and Circuits)*, Honolulu, HI, USA, June 16-20, 2024; IEEE, 2024, pp 1-2. DOI
3. Chiu, C.; De, S.; Cho, C.; Hou, T. Trade-off between thermal budget and thickness scaling: a bottleneck on quest for BEOL compatible ultra-thin ferroelectric films sub-5nm. In *2024 8th IEEE Electron Devices Technology & Manufacturing Conference (EDTM)*, Bangalore, India, March 3-6, 2024; IEEE, 2024, pp 1-3. DOI
4. Lyu, X.; Si, M.; Sun, X.; Capano, M. A.; Wang, H.; Ye, P. Ferroelectric and anti-ferroelectric hafnium zirconium oxide: scaling limit, switching speed and record high polarization density. In *2019 Symposium on VLSI Technology*, Kyoto, Japan, June 9-14, 2019; IEEE, 2019, pp T44-5. DOI
5. Song, K.; Kim, D.; Kim, D.; et al. Fatigue-free ferroelectric HZO operable at 1V with > 10_{12} endurance via precycling pulse engineering. In *2025 IEEE International Electron Devices Meeting (IEDM)*, San Francisco, CA, USA, December 6-10, 2025; IEEE, 2025, pp 1-4. DOI
6. Liu, X.; Geng, X.; Liu, H.; et al. Recent progress and applications of HfO_2-based ferroelectric memory. *Tsinghua. Sci. Technol.* **2023**, *28*, 221-9. DOI
7. Liao, J.; Dai, S.; Peng, R.; et al. HfO_2-based ferroelectric thin film and memory device applications in the post-Moore era: a review. *Fundam. Res.* **2023**, *3*, 332-45. DOI
8. Zhu, Z.; Zhang, B.; Zheng, Y. Progress on hafnium oxide-based emerging ferroelectric materials and applications. *Microstructures* **2025**, *5*, 2025095. DOI
9. Shao, M.; Zhao, R.; Liu, H.; et al. Challenges and recent advances in HfO_2-based ferroelectric films for non-volatile memory applications. *Chip* **2024**, *3*, 100101. DOI
10. Zhou, Z.; Li, L.; Feng, Y.; et al. Advancing the frontiers of HfO_2-based ferroelectric memories: innovative concepts from materials to applications. *Adv. Mater.* **2025**, *37*, e09525. DOI
11. Ramaswamy, N.; Calderoni, A.; Zahurak, J.; et al. NVDRAM: A 32Gb dual layer 3D stacked non-volatile ferroelectric memory with near-DRAM performance for demanding AI workloads. In *2023 International Electron Devices Meeting (IEDM)*, San Francisco, CA, USA, December 9-13, 2023; IEEE, 2023, pp 1-4. DOI
12. Khosla, R.; Sharma, S. K. Integration of ferroelectric materials: an ultimate solution for next-generation computing and storage devices. *ACS. Appl. Electron. Mater.* **2021**, *3*, 2862-97. DOI
13. Kim, M.; Kim, I.; Lee, J. CMOS-compatible ferroelectric NAND flash memory for high-density, low-power, and high-speed three-dimensional memory. *Sci. Adv.* **2021**, *7*, eabe1341. DOI PubMed PMC
14. Park, H.; Han, C.; Choi, Y.; Choi, M.; Won, S.; Shin, C. Effect of bottom electrode annealing temperature and atmosphere on endurance characteristics of ferroelectric $Hf_{0.5}Zr_{0.5}O_2$ Capacitors. *IEEE. Electron. Device. Lett.* **2025**, *46*, 2038-41. DOI
15. Han, C.; Ryun Kwon, K.; Jeong, S.; et al. Tunable ferroelectric properties of HfO_2-based oxides: role of aluminum doping and bottom electrodes. *IEEE. Trans. Electron. Devices.* **2025**, *72*, 635-9. DOI
16. Park, H. S.; Shin, J. C.; Kim, K. D.; et al. Enhancing ferroelectric properties of $Hf_{0.5}Zr_{0.5}O_2$ thin films using the HfN/TiN and W/TiN bi-layer bottom electrodes. *J. Materiomics.* **2025**, *11*, 101109. DOI
17. Tierno, D.; Croes, K.; Ajaykumar, A.; Ramesh, S.; Van Den Bosch, G.; Rosmeulen, M. Reliability of Mo as word line metal in 3D NAND. In *2021 IEEE International Reliability Physics Symposium (IRPS)*, Monterey, CA, USA, March 21-25, 2021; IEEE, 2021, pp 1-6. DOI
18. Erofeev, I.; Hartanto, A. W.; Saidov, K.; et al. Solving the annealing of Mo interconnects for next-gen integrated circuits. *Adv. Electron. Mater.* **2024**, *10*, 2400035. DOI
19. Ajaykumar, A.; Breuil, L.; Katcko, K.; et al. First demonstration of ruthenium and molybdenum word lines integrated into 40 nm pitch 3D-NAND memory devices. In *2021 Symposium on VLSI Technology*, Kyoto, Japan, June 13-19, 2021; 2021; IEEE, pp 1-2. https://ieeexplore.ieee.org/document/9508691.
20. Zhao, B.; Sun, K.; Song, Z.; Yang, J. Ultrathin Mo/MoN bilayer nanostructure for diffusion barrier application of advanced Cu metallization. *Appl. Surf. Sci.* **2010**, *256*, 6003-6. DOI
21. Founta, V.; Soulié, J.; Sankaran, K.; et al. Properties of ultrathin molybdenum films for interconnect applications. *Materialia* **2022**, *24*, 101511. DOI
22. Wang, W.; Xiong, F.; Zhu, S.; Chen, J.; Xie, J.; An, Q. Defect engineering in molybdenum-based electrode materials for energy storage. *eScience* **2022**, *2*, 278-94. DOI
23. Kim, S. E.; Sung, J. Y.; Jeon, J. D.; et al. Toward advanced high-*k* and electrode thin films for DRAM capacitors via atomic layer deposition. *Adv. Mater. Technol.* **2022**, *8*, 2200878. DOI

24. Zhao, R.; Liu, T.; Zhao, X.; et al. Impact of molybdenum oxide electrode on the ferroelectricity of doped-Hafnia oxide capacitors. *IEEE. Trans. Electron. Devices.* **2022**, *69*, 1492-6. DOI
25. Lee, Y.; Kim, S. H.; Jeong, H. W.; et al. Mitigation of field-driven dynamic phase evolution in ferroelectric $Hf_{0.5}Zr_{0.5}O_2$ films by adopting oxygen-supplying electrode. *Appl. Surf. Sci.* **2024**, *648*, 158948. DOI
26. Reddy, P. S.; Nallagatla, V. R.; Sreedhar, A. Enhanced remnant polarization in ferroelectric $Hf_{0.5}Zr_{0.5}O_2$ thin film capacitors through Mo top electrode by post-metallization annealing treatment. *Physica. B:. Condensed. Matter.* **2024**, *685*, 416024. DOI
27. Jacobson, D. L.; Campbell, A. E. Molybdenum work function determined by electron emission microscopy. *Metall. Trans*. **1971**, *2*, 3063-6. DOI
28. Berge, S.; Gartland, P.; Slagsvold, B. Photoelectric work function of a molybdenum single crystal for the (100), (110), (111), (112), (114), and (332) faces. *Surf. Sci.* **1974**, *43*, 275-92. DOI
29. Lee, W.; Cho, C. J.; Lee, W. C.; Hwang, C. S.; Chang, R. P. H.; Kim, S. K. MoO_2 as a thermally stable oxide electrode for dynamic random-access memory capacitors. *J. Mater. Chem. C.* **2018**, *6*, 13250-6. DOI
30. Inzani, K.; Nematollahi, M.; Vullum-bruer, F.; Grande, T.; Reenaas, T. W.; Selbach, S. M. Electronic properties of reduced molybdenum oxides. *Phys. Chem. Chem. Phys.* **2017**, *19*, 9232-45. DOI
31. Ranade, P.; Takeuchi, H.; King, T.; Hu, C. Work function engineering of molybdenum gate electrodes by nitrogen implantation. *Electrochem. Solid-State. Lett.* **2001**, *4*, G85. DOI
32. Nam, H.; Shin, C. Study of high-k/metal-gate work-function variation using Rayleigh distribution. *IEEE. Electron. Device. Lett.* **2013**, *34*, 532-4. DOI
33. Lin, S.; Lai, Y. Effect of nitrogen on the physical properties and work function of MoN_x cap layers on HfO_2 gate dielectrics. *ECS. J. Solid. State. Sci. Technol.* **2014**, *3*, N161-5. DOI
34. Zhang, Q.; Ma, J.; Lei, M.; Quhe, R. Metallic MoN layer and its application as anode for lithium-ion batteries. *Nanotechnology* **2018**, *29*, 165402. DOI
35. Kang, W.; Ahn, J. S.; Lee, J. H.; Choi, B. J.; Han, J. H. Enhanced oxidation resistance and interface stability of atomic-layer-deposited MoN_x electrodes via TiN passivation for DRAM cell capacitor applications. *ACS. Appl. Mater. Interfaces.* **2024**, *16*, 57446-56. DOI
36. Tsui, B.; Huang, C.; Lu, C. Investigation of molybdenum nitride gate on SiO_2 and HfO_2 for MOSFET application. *J. Electrochem. Soc.* **2006**, *153*, G197. DOI
37. Nečas, D.; Klapetek, P. Gwyddion: an open-source software for SPM data analysis. *Open. Phys.* **2012**, *10*, 181-8. DOI
38. Müller, J.; Böscke, T. S.; Schröder, U.; et al. Ferroelectricity in simple binary ZrO_2 and HfO_2. *Nano. Lett.* **2012**, *12*, 4318-23. DOI
39. Reed, T. B. *Free energy of formation of binary compounds.* MIT press Cambridge, MA, **1971**.
40. Kubaschewski, O.; Alcock, C. B. *Metallurgical thermochemistry,* 5th ed; Pergamon Press, **1979**.
41. Lajaunie, L.; Boucher, F.; Dessapt, R.; Moreau, P. Quantitative use of electron energy-loss spectroscopy Mo-M2,3 edges for the study of molybdenum oxides. *Ultramicroscopy* **2015**, *149*, 1-8. DOI
42. Soto, G.; De La Cruz, W.; Farías, M. XPS, AES, and EELS characterization of nitrogen-containing thin films. *J. Electron. Spectrosc. Relat. Phenom.* **2004**, *135*, 27-39. DOI
43. Chase Jr, M. W. JANAF thermochemical tables. *J. Phys. Chem. Ref. Data.* **1985**. DOI
44. Vickerman, J. C.; Briggs, D. ToF-SIMS: materials analysis by mass spectrometry; Im publications, **2013**.
45. Cho, D.; Jung, H. S.; Yu, I.; et al. Stabilization of tetragonal HfO_2 under low active oxygen source environment in atomic layer deposition. *Chem. Mater.* **2012**, *24*, 3534-43. DOI
46. Jaffe, J. E.; Bachorz, R. A.; Gutowski, M. Low-temperature polymorphs of ZrO_2 and HfO_2: a density-functional theory study. *Phys. Rev. B.* **2005**, *72*, 144107. DOI
47. Böscke, T. S.; Teichert, S.; Bräuhaus, D.; et al. Phase transitions in ferroelectric silicon doped hafnium oxide. *Appl. Phys. Lett.* **2011**, *99*, 112904. DOI
48. Fields, S. S.; Smith, S. W.; Fancher, C. M.; et al. Metal nitride electrode stress and chemistry effects on phase and polarization response in ferroelectric $Hf_{0.5}Zr_{0.5}O_2$ thin films. *Adv. Mater. Inter.* **2021**, *8*, 2100018. DOI
49. Yang, K.; Choi, H.; Ahn, J. S.; et al. Utilization of oxygen content modulated Ru electrode to examine the interfacial redox chemistry of ferroelectric $Hf_{0.5}Zr_{0.5}O_2$. *J. Materiomics.* **2025**, *11*, 101110. DOI
50. Li, Y.; Liang, R.; Xiong, B.; et al. $TiN_x/Hf_{0.5}Zr_{0.5}O_2/TiN_x$ ferroelectric memory with tunable transparency and suppressed wake-up effect. *Appl. Phys. Lett.* **2019**, *114*, 052902. DOI
51. Dang, Z.; Lv, S.; Gao, Z.; et al. Improved endurance of $Hf_{0.5}Zr_{0.5}O_2$-based ferroelectric capacitor through optimizing the Ti-N ratio in TiN electrode. *IEEE. Electron. Device. Lett.* **2022**, *43*, 561-4. DOI

52. Pešić, M.; Fengler, F. P. G.; Larcher, L.; et al. Physical mechanisms behind the field-cycling behavior of HfO_2-based ferroelectric capacitors. *Adv. Funct. Mater.* **2016**, *26*, 4601-12. DOI
53. Degraeve, R.; Groeseneken, G.; Bellens, R.; et al. New insights in the relation between electron trap generation and the statistical properties of oxide breakdown. *IEEE. Trans. Electron. Devices.* **1998**, *45*, 904-11. DOI
54. Wang, X.; Feng, Y.; He, Y.; et al. Sub-10 nm fully atomic-layer-deposited MFM stack with enhanced reliability: record-low $I_{leakage}$ and record-high E_{BD} in 3 nm ferroelectric HZO. In *2025 IEEE International Electron Devices Meeting (IEDM)*, San Francisco, CA, USA, December 6-10, 2025; IEEE, 2025, pp 1-4. DOI

Disclaimer/Publisher's Note: All statements, opinions, and data contained in this publication are solely those of the individual author(s) and contributor(s) and do not necessarily reflect those of OAE and/or the editor(s). OAE and/or the editor(s) disclaim any responsibility for harm to persons or property resulting from the use of any ideas, methods, instructions, or products mentioned in the content.

© The Author(s) 2026. Open Access This article is licensed under a Creative Commons Attribution 4.0 International License (https://creativecommons.org/licenses/by/4.0/), which permits unrestricted use, sharing, adaptation, distribution and reproduction in any medium or format, for any purpose, even commercially, as long as you give appropriate credit to the original author(s) and the source, provide a link to the Creative Commons license, and indicate if changes were made.